J Comput Neurosci (2008) 24:358–373
DOI 10.1007/s10827-007-0060-8

Parameter estimation for bursting neural models

Joseph H. Tien · John Guckenheimer

Received: 24 January 2007 / Revised: 6 September 2007 / Accepted: 15 October 2007 / Published online: 13 November 2007

Abstract This paper presents work on parameter estimation methods for bursting neural models. In our approach we use both geometrical features specific to bursting, as well as general features such as periodic orbits and their bifurcations. We use the geometry underlying bursting to introduce defining equations for burst initiation and termination, and restrict the estimation algorithms to the space of bursting periodic orbits when trying to fit periodic burst data. These geometrical ideas are combined with automatic differentiation to accurately compute parameter sensitivities for the burst timing and period. In addition to being of inherent interest, these sensitivities are used in standard gradient-based optimization algorithms to fit model burst duration and period to data. As an application, we fit Butera et al.'s (*Journal of Neurophysiology* 81, 382–397, 1999) model of preBötzinger complex neurons to empirical data both in control conditions and when the neuromodulator norepinephrine is added (Viemari and Ramirez, *Journal of Neurophysiology* 95, 2070–2082, 2006). The results suggest possible modulatory mechanisms in the preBötzinger complex, including modulation of the persistent sodium current.

Keywords Respiration · Hodgkin–Huxley · Multiple time scales

Electronic Supplementary Material The online version of this article (doi:10.1007/s10827-007-0060-8) contains supplementary material, which is available to authorized users.

Action Editor: Nicolas Brunel

J. H. Tien (✉)
Center for Applied Mathematics, Cornell University,
Ithaca, NY 14853, USA
e-mail: joetien@gmail.com

J. Guckenheimer
Mathematics Department, Cornell University,
Ithaca, NY 14853, USA
e-mail: jmg16@cornell.edu

1 Introduction

Parameter estimation for neural models is an important but challenging task. Fitting Hodgkin–Huxley style models to data helps discern the roles of different ion currents in shaping a cell's firing pattern, suggests different modulatory mechanisms, and can aid in characterizing currents which are difficult to measure. Research on automated methods for parameter estimation is ongoing (Bhalla and Bower 1993; Foster et al. 1993; Hayes et al. 2005; Prinz et al. 2003; Tabak et al. 2000; Vanier and Bower 1999). Local minima in the objective function landscape as well as numerical challenges such as the lack of analytic gradients are two difficulties which are especially salient for bursting models. Spike and burst timing discrepancies between burst trajectories can result in complicated objective function landscapes with many local minima. Bursting models possess multiple time scales, which can lead to delicate canard trajectories (Terman 1991). These can cause rapid changes in the objective function landscape and contribute to numerical difficulties. Little work has been done on using smooth, local optimization methods for burst parameter estimation. Instead, either non-smooth methods (Bhalla and Bower 1993; Vanier and Bower 1999) or database construction and searching (Prinz et al. 2003) have been used. This paper

presents a local method for parameter estimation which uses geometrical features underlying bursting to aid in estimation.

Geometric features of bursting ODE models are present both in multiple time scale features (Rinzel and Lee 1987), and in general dynamical structures such as periodic orbits. We use the former to define when a burst initiates and terminates, and the latter to restrict to periodic model solutions when fitting periodic data. Focusing on coarse burst features such as burst duration and period leads to simpler objective function landscapes. Smooth local methods require gradients of the objective function. Here this means computing the gradients of burst initiation and termination timing, and of the burst period. These quantities can change sharply when spikes are added or subtracted from a burst. We use automatic differentiation and Taylor series integration to improve numerical accuracy of these calculations. The gradients are themselves of biological interest. They give the parameter sensitivities of burst timing and period, and thus can help determine the roles of different currents in shaping burst characteristics. We illustrate these ideas by examining respiratory preBötzinger neurons. We fit Butera et al.'s (1999) model to empirical data measured by Viemari and Ramirez (2006), and use our algorithms to look at the role of the persistent sodium current ($I_{\mathrm{Na(P)}}$). We also examine possible modulatory targets in the preBötzinger complex (pBC).

Rinzel and Lee's (1987) fast-slow "dissection" of bursting models contributed greatly to understanding burst mechanisms. This dissection is based upon geometrical features associated with partitioning the model into fast and slow subsystems. We use this same geometry to introduce defining equations for burst initiation and termination. This is discussed in Section 2.2. In many situations, rhythmic bursting is observed and periodic model solutions are desired. Casey (2004) introduced optimization algorithms specifically for periodic orbits, and applied them to spiking neural models. We build upon Casey's work by developing optimization algorithms for estimating parameters of models with periodic burst trajectories. We fit data to characteristics derived from the fast-slow dissection of the model trajectories. Exploiting these features of the ODEs in optimization algorithms is largely unexplored. This approach considerably simplifies landscapes compared to using least squares on the entire voltage trace.

These geometric ideas can be implemented numerically in a variety of ways. This includes different methods for calculating gradients, as analytic gradients of the flow maps for ODE models are seldom available in closed form. Finite differences are a common and easily implemented choice. We describe here an alternative approach which uses automatic differentiation together with Taylor series integration to calculate derivatives of the flow (Griewank 2000). Combining this with our burst defining equations provides an accurate method for computing the parameter sensitivities of burst timing, duration, and period. These methods are discussed in Section 2.3.

Breathing is a heavily modulated periodic rhythm which involves bursting neurons. The preBötzinger complex (pBC) is a functionally defined region of the brainstem that plays a key role in respiratory rhythm generation (Feldman et al. 2003; Onimaru et al. 1989; Smith et al. 1991). Premotor neurons in the pBC project to motor neurons innervating the hypoglossal nerve. Electrical bursts in the hypoglossal nerve correspond to inspiration via movement of the tongue to clear the air passage. The pBC maintains rhythmic activity similar to hypoglossal nerve electrical activity in the intact system even when excised from the rest of the ventral respiratory group (Smith et al. 1991). Lesions to the pBC disrupt the breathing rhythm (Feldman et al. 2003). Thus the pBC is essential for normal respiratory rhythm generation. The pBC contains a variety of cell types, including endogenous bursting cells which continue to burst when synaptically isolated. Understanding how the constituent ion currents of these endogenous bursters influence burst characteristics is of interest, particularly as these cells have been proposed to serve as pacemakers for the pBC rhythm (Johnson et al. 1994; Koshiya and Smith 1999; Onimaru et al. 1989; Smith et al. 1991).

Butera et al. (1999) presented a model of pBC neurons containing a minimal set of currents. Viemari and Ramirez (2006) measured burst characteristics of isolated endogenous bursting pBC neurons both in control conditions and in the presence of the neuromodulator norepinephrine. Firing patterns in the pBC can be modulated in a variety of ways. For example, burst duration may be altered independent of burst period, or burst period may change while burst duration is held constant (Viemari and Ramirez 2006). By using our optimization algorithms to fit Butera et al.'s model to the empirical measurements of Viemari and Ramirez, we can examine the role of different model currents and identify possible modulatory targets in the pBC. This includes the persistent sodium current ($I_{\mathrm{Na(P)}}$), which is found in many mammalian structures (see Crill 1996 and Magistretti and Alonso 1999 for listings). The persistent sodium current plays many functional roles including burst generation (such as in the pBC), bistability and plateau potential generation, and excitatory postsynaptic potential amplification (Deisz et al. 1991).

Despite its importance, the persistent sodium current is poorly characterized in many systems, including in the pBC.

2 Methods

2.1 Objective functions

Optimization methods try to minimize an objective function. In the context of parameter estimation, the objective function gives some measure of the goodness of fit of a model to data. Different objective function choices have been considered in the literature (Bhalla and Bower 1993; Vanier and Bower 1999). Here the focus is on fitting burst duration and period. We use objective functions of the form

$$G = (X - X_{\text{ref}})^2 + \left(w \log \frac{Y_{\text{ref}}}{Y} \right)^2. \tag{1}$$

Thus the objective function G consists of the squared residuals of X together with a log penalty for discrepancies in Y, with w the penalty weight. In the remainder of this paper either X will be the burst period and Y the burst duration, or X the burst duration and Y the burst period. Fitting only one of these quantities is done by setting $w = 0$. When fitting both burst duration and period, a heuristic for choosing w is that proportional changes in X and Y result in comparable changes in G near $(X_{\text{ref}}, Y_{\text{ref}})$. We estimate w as follows. Let μ denote a common proportional deviation of X and Y from their reference values. Then $X = (1+\mu)X_{\text{ref}}$, $Y = (1+\mu)Y_{\text{ref}}$, and $G = (\mu X_{\text{ref}})^2 + \left(w \log(1+\mu)\right)^2$. Setting $\mu X_{\text{ref}} = w \log(1+\mu)$ gives $w = \frac{\mu X_{\text{ref}}}{\log(1+\mu)} \approx X_{\text{ref}}$. Thus $w = X_{\text{ref}}$ under this heuristic.

We use gradient-based methods to minimize G. Thus we need to calculate the burst duration and period for our model, together with the derivatives with respect to parameters of these quantities.

Note that G is only defined for bursting periodic solutions. We use an infinite barrier method (Fletcher 1987) to restrict to the periodic burst domain. This corresponds to setting $G = \infty$ when periodic burst solutions do not exist.

2.2 Burst defining equations

As initiated by Rinzel and Lee (1987), bursting models can be examined from a multiple time scale viewpoint. Consider a system of ODEs of the form

$$\begin{aligned} \dot{x} &= f(x, y, \epsilon) \\ \dot{y} &= \epsilon g(x, y, \epsilon), \end{aligned} \tag{2}$$

where $x \in \mathbb{R}^m$, $y \in \mathbb{R}^n$, and ϵ is a small positive parameter. The phase space variable x corresponds to the fast variables, and y the slow variables. Considering the singular limit $\epsilon \to 0$ gives the fast subsystem, with the slow variables y treated as parameters. The collection of fixed points of the fast subsystem is called the critical manifold $\mathcal{M}_0$ (Jones 1995). During the quiescent phase of a burst, the system lies close to a stable, hyperpolarized component of $\mathcal{M}_0$. Spike initiation corresponds to rapidly moving away from this stable component of $\mathcal{M}_0$ and closely following a family of fast subsystem periodic orbits. Burst termination corresponds to returning close to a stable component of $\mathcal{M}_0$.

We use this as the basis for our burst initiation and termination defining equations. Let $z = (x, y)^T$ denote the phase space variables. The burst initiation and termination event functions $\Gamma_{\text{init}}(z)$, $\Gamma_{\text{term}}(z)$ will be monitored over solution trajectories, with the beginning and end of a burst corresponding to places where Γ_{init} and Γ_{term} are respectively equal to zero.

We define burst initiation as crossing a voltage threshold while in the silent phase:

$$\Gamma_{\text{init}}(z) = \pi_v(z) - v_{\text{init}}. \tag{3}$$

Here π_v denotes projection to the voltage coordinate and v_{init} is the chosen voltage threshold.

For burst termination, we use the defining equation

$$\Gamma_{\text{term}}(z) = \frac{1}{2}\|Sf(z)\|_2^2 - \delta, \tag{4}$$

together with the requirement that $\dot{\Gamma}_{\text{term}} < 0$. This corresponds to entry into a neighborhood of $\mathcal{M}_0$, where S is a diagonal scaling matrix and the size of the neighborhood depends upon the user-defined parameter δ. There is the additional requirement that the system passes close to a stable component of M_0 and not, for example, close to a saddle component. This can be accomplished by taking a proposed event point, locating a point on M_0 which minimizes the distance to the proposed event point, and then checking the stability of the point on M_0.

These event defining equations are depicted in Fig. 1. The time spent between crossing these event surfaces is

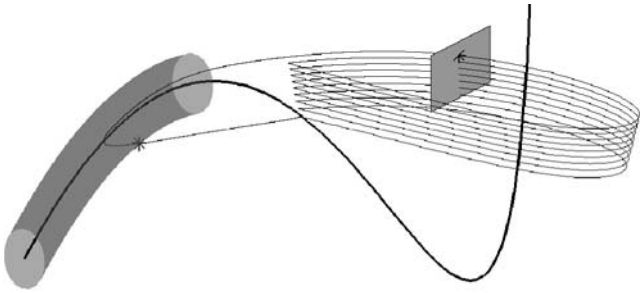

Fig. 1 Schematic of burst event surfaces. Burst initiation corresponds to crossing the planar cross-section, and burst termination corresponds to entering the gray tube. The *heavy line* depicts the critical manifold M_0, the *lighter line* is the burst periodic orbit, and event points are marked by asterisks

the burst duration, which is one of the features to be fit in the optimization.

2.3 Computing solution trajectories and sensitivities

In this section $z \in \mathbb{R}^{zdim}$ denotes phase space points, $\lambda \in \mathbb{R}^p$ denotes the ODE parameters, and f denotes the (full) vector field. Thus $\dot{z} = f(z, \lambda)$ is our neural model.

We use automatic differentiation and Taylor series integration to compute solution trajectories and their derivatives. We use a shooting framework introduced by Guckenheimer and Meloon (2000) to compute periodic orbits. Burst solution trajectories can be computed as the zeros of shooting maps, as we now describe. Let Δ be a discrete curve representation of our solution trajectory. Δ is a collection of time and phase space points, some of which are event points and some of which are not. Let $(t_0, z_0), \ldots, (t_m, z_m)$ be points on a solution trajectory. We take $t_0 = 0$ by convention. For periodic solutions, we also have $z_m = z_0$. This gives

$$\Delta = (t_1, \ldots, t_m, z_0, \ldots, z_{m-1}). \tag{5}$$

Suppose there are n_e points (t, z) at which Γ_{init} or Γ_{term} is equal to zero. Let $\sigma_1, \ldots, \sigma_{n_e}$ denote the indices of these burst event points. In the simplest situation for burst periodic orbits, $n_e = 2$.

The shooting map $F : \mathbb{R}^{(zdim+1)\cdot m} \times \mathbb{R}^p \to \mathbb{R}^{zdim\cdot m+n_e}$ is defined as:

$$F(\mathbf{t}, \mathbf{z}, \lambda) = \begin{pmatrix} \Phi(z_0, t_1) - z_1 \\ \Phi(z_1, t_2 - t_1) - z_2 \\ \vdots \\ \Phi(z_{m-1}, t_m - t_{m-1}) - z_0 \\ \Gamma_{\sigma_1}(z_{\sigma_1}) \\ \vdots \\ \Gamma_{\sigma_{n_e}}(z_{\sigma_{n_e}}) \end{pmatrix}, \tag{6}$$

where Φ is the flow map for the system and the Γ_{σ_i} correspond to burst initiation or termination defining functions as appropriate (Section 2.2). For notational convenience we have suppressed the λ dependence of Φ and Γ. Burst solutions to the ODE correspond to zeros of the equation

$$F\big(\Delta(\lambda), \lambda\big) = 0. \tag{7}$$

The first m components of Eq. (7) say that Δ is a periodic solution to the ODE. The last n_e components of Eq. (7) specify that the points $(t_{\sigma_i}, z_{\sigma_i}), i = 1, \ldots, n_e$ are burst event points.

Differentiating Eq. (7) with respect to parameters λ gives:

$$D_\Delta F \cdot D_\lambda \Delta + D_\lambda F = 0. \tag{8}$$

$D_\lambda \Delta$, the derivative of the solution trajectory with respect to parameters, is the quantity of interest. While closed form expressions for the flow maps $\Phi(z_i, t_{i+1} - t_i)$ in Eq. (6) are not available, we can use automatic differentiation and Taylor series integration to compute both Φ and the derivatives of Φ with respect to phase space variables and to parameters. Using automatic differentiation allows us to compute these derivatives to high accuracy, essentially to the same accuracy as Φ. Thus we can compute $D_\Delta F$ and $D_\lambda F$ to high accuracy. This in turn allows us to accurately compute $D_\lambda \Delta$ by solving for $D_\lambda \Delta$ in Eq. (8), provided that $D_\Delta F$ is square and non-singular. Unfortunately F as defined in Eq. (6) is not square. However, the situation can be remedied by appending the tangent vectors which correspond to sliding non-event mesh points along the periodic orbit. Let $f(z_i)$ denote the (full) vector field at point z_i. Tangent vectors for sliding all mesh points along the orbit are given by:

$$\begin{aligned} v_0 &= \big(f(z_0)^T, 0, \ldots, -1, -1, \ldots, -1, 0\big)^T, \\ v_1 &= \big(0, f(z_1)^T, \ldots, 0, 1, 0, \ldots, 0\big)^T, \\ &\vdots \\ v_{m-1} &= \big(0, \ldots, f(z_{m-1})^T, 0, \ldots, 1, 0\big)^T. \end{aligned} \tag{9}$$

See Guckenheimer and Meloon (2000). Let $\rho_1, \ldots, \rho_{m-n_e}$ denote the indices of non-event points. Then appending $v_{\rho_1}^T, \ldots, v_{\rho_{m-n_e}}^T$ to $D_\Delta F$ gives a

square matrix. Letting $D_i = D_z\Phi(z_i, t_{i+1} - t_i)$ and $\hat{f}_i = f(\Phi(z_{i-1}, t_i - t_{i-1}))$ we have

$$D_\Delta F = \begin{pmatrix} D_0 & -Id & & & \hat{f}_1 \\ & \ddots & & & \ddots \\ -Id & & D_{m-1} & & \hat{f}_m \\ & \nabla\Gamma^T_{\sigma_1} & & & \\ & & \ddots & & \\ & & & \nabla\Gamma^T_{\sigma_{n_e}} & \\ v^T_{\rho_1} & & & & \\ & & \ddots & & \\ & & & v^T_{\rho_{m-n_e}} & \end{pmatrix}. \tag{10}$$

The D_i and Id blocks lie in $\mathbb{R}^{zdim \times zdim}$.

It can be shown that $D_\Delta F$ has full rank when evaluated at a periodic orbit with transverse events and a single multiplier of modulus 1. The interested reader is referred to the Appendix for details. Provided that the periodic orbit is not undergoing a bifurcation and the events are transverse, we can compute $D_\lambda \Delta$ by

$$D_\lambda \Delta = -(D_\Delta F)^{-1} D_\lambda F. \tag{11}$$

Zeros of F correspond to periodic burst solutions to the ODE. There are different possibilities for finding $\Delta(\lambda)$ which satisfy Eq. (7). We found a simple shooting method to work well here. A Poincare cross-section was placed based upon a slow variable value during the quiescent phase, and zeros of the return map were found by Newton's method. Finite differences were used to compute the Jacobian of the return map. After a periodic orbit was located, Taylor series integration with automatic differentiation was used to compute the derivatives of the flow around the periodic orbit, and thus to obtain the parameter sensitivities of the trajectories (11). The alternative of using finite differences to compute these sensitivities is less accurate.

Parameter sensitivities give information on the relative importance of different parameters in determining a trajectory characteristic. This information can be expressed in terms of scaled parameter sensitivities. Let ξ be a trajectory characteristic of interest, λ_i a parameter, and $\bar{\lambda}_i$ the characteristic scale of λ_i. Then $\frac{\partial \xi}{\partial \lambda_i} \cdot \bar{\lambda}_i$ is the scaled sensitivity of ξ to λ_i. The scaled sensitivities measure the relative effects of small proportional changes in the parameters. This information highlights changes that have a large effect on ξ. Infinitesimal parameter changes in directions normal to $D_\lambda \Delta$ leave ξ unchanged.

2.4 PreBötzinger complex

2.4.1 The model of Butera, Rinzel, and Smith

Cells in the pBC contain a number of different ion channels, not all of which are necessary for endogenous bursting. Butera et al. (1999) developed a Hodgkin–Huxley style model for pBC cells which includes a minimal set of currents: a fast sodium current I_{Na}, a delayed rectifier potassium current I_{K}, a persistent sodium current $I_{\mathrm{Na(P)}}$, and a leak current I_L. The model equations are:

$$C\dot{v} = -I_{\mathrm{Na}} - I_{\mathrm{K}} - I_{\mathrm{Na(P)}} - I_L \tag{12}$$

$$I_{\mathrm{Na}} = g_{\mathrm{Na}} m_\infty^3 (1 - n)(v - v_{\mathrm{Na}}) \tag{13}$$

$$I_{\mathrm{K}} = g_{\mathrm{K}} n^4 (v - v_{\mathrm{K}}) \tag{14}$$

$$I_{\mathrm{Na(P)}} = g_{\mathrm{Na(P)}} \hat{m}_\infty h (v - v_{\mathrm{Na(P)}}) \tag{15}$$

$$I_L = g_{\mathrm{L}}(v - v_{\mathrm{L}}). \tag{16}$$

The membrane potential is given by v, and $m, n, \hat{m}$, and h are gating variables (Table 1). m and n are activation variables for the fast sodium and delayed rectifier potassium channels, while $\hat{m}$ and h are the activation and inactivation variables for the persistent sodium channel. The variable n also serves as the inactivation variable for the fast sodium channel. Equations for the gating variables share a common form:

$$\dot{x} = \frac{x_\infty - x}{\tau_x} \tag{17}$$

$$x_\infty(v) = \frac{1}{1 + \exp\left(\frac{v - \theta_x}{\sigma_x}\right)} \tag{18}$$

$$\tau_x(v) = \frac{\bar{\tau}_x}{\cosh\left(\frac{v - \theta_x}{2\sigma_x}\right)}. \tag{19}$$

Each gating variable is associated with three parameters, $\theta, \bar{\tau}$, and σ. x_∞ denotes the steady state value for gating variable x when the voltage is held fixed. θ is the half-activation value ($x_\infty(\theta) = \frac{1}{2}$), and σ gives the steepness of the steady state activation curve when evaluated at θ. The sign of σ indicates whether the steady state value x_∞ increases (negative σ) or decreases with voltage. For a fixed voltage, gating

Table 1 Phase space variables for system (12–19)

v	Membrane potential (mV)
t	Time (ms)
m	Fast sodium activation
n	Potassium activation and fast sodium inactivation
$\hat{m}$	Persistent sodium activation
h	Persistent sodium inactivation

Table 2 Parameters for system (12–19) (Butera et al. 1999)

C	Membrane capacitance	21 pF
g_{Na}	Maximal fast sodium conductance	28 nS
v_{Na}	Fast sodium reversal potential	50 mV
θ_m	m half-activation	−34 mV
σ_m	m time scale half-width	−5 mV
g_K	Maximal potassium conductance	11.2 nS
v_K	Potassium reversal potential	−85 mV
θ_n	n half-activation	−29 mV
σ_n	n time scale half-width	−4 mV
$\bar{\tau}_n$	n time scale constant	10 ms
$g_{Na(P)}$	Maximal persistent sodium conductance	2.8 nS
$v_{Na(P)}$	Persistent sodium current reversal potential	50 mV
$\theta_{\hat{m}}$	$\hat{m}$ half-activation	−40 mV
$\sigma_{\hat{m}}$	$\hat{m}$ time scale half-width	−6 mV
θ_h	h half-activation	−48 mV
σ_h	h time scale half-width	6 mV
$\bar{\tau}_h$	h time scale constant	1×10^4 ms
g_L	Maximal leak conductance	2.8 nS
v_L	Leak reversal potential	−60 mV

variables approach their steady state values x_∞ exponentially at a rate $\tau(v)$. The value of $\tau(v)$ is given by a bell-shaped curve with peak of height $\bar{\tau}$ centered at θ and half-width given by σ (Butera et al. 1999).

Table 2 lists the units and default values of the parameters for system (12–19). Butera et al. (1999) also include an external applied current and a tonic excitatory synaptic current. We omit these because they can be absorbed into the leak current.

2.4.2 *Empirical burst data and preBötzinger neuromodulation*

Viemari and Ramirez (2006) measured burst characteristics for synaptically isolated pBC pacemaker cells, both under control conditions and in the presence of norepinephrine. Norepinephrine is a respiratory system neuromodulator that plays an important role in responses to elevated carbon dioxide levels (Kinkead et al. 2001). Different effects were observed for Cd^{2+}-sensitive versus Cd^{2+}-insensitive pacemakers. Bursting in Cd^{2+}-sensitive cells is calcium dependent, whereas Cd^{2+}-insensitive bursting is thought to rely upon the persistent sodium current. Norepinephrine altered Cd^{2+}-insensitive pacemaker burst period, but did not affect burst duration. In contrast, Cd^{2+}-sensitive pacemaker burst duration was modulated but burst period was unaffected. Both α_1 and α_2 noradrenergic receptors affect respiratory output through G protein coupled pathways (Hille 2001; Johnson et al. 1994; Viemari and Ramirez 2006). Norepinephrine acts on synaptically isolated Cd^{2+}-sensitive pacemakers through an α_1-receptor mediated effect on calcium dependent channels (Viemari and Ramirez 2006). The modulatory target for Cd^{2+}-insensitive pacemakers is not known. The empirical data is given in Table 3. We use our optimization algorithms to fit Butera et al.'s model to the data of Viemari and Ramirez. As system (12–19) does not include calcium, we focus on fitting the Cd^{2+}-insensitive data.

Many pBC neuromodulators affect K^+ channels, often through G protein coupled pathways. The binding of serotonin to 5-HT1A receptors activates inward rectifier potassium channels K_{ir} (Richter et al. 2003). K_{ATP} channels in the plasmalemma are involved in short term respiratory depression following hypoxia (Haller et al. 2001), and mitochondrial K_{ATP} channels are conjectured to play a role in long term facilitation following repeated hypoxic episodes (Mironov et al. 2005). Serotonin binding of 5-HT4 receptors also affects I_h activity via cAMP-mediated phosphorylation (Bickmeyer et al. 2002). Brain derived neurotrophic factor (BDNF) also modulates I_h. Thoby-Brisson et al. (2003) showed that BDNF application both decreased I_h conductance and shifted I_h activation curves to more hyperpolarized voltages in neonatal mice. The pH-sensitive TASK channels are another group of K^+ channels which are modulatory targets in the pBC (Washburn et al. 2003, 2002). TASK-1 and TASK-3 channels are expressed in the rat pBC (Washburn et al. 2003). These channels are sensitive to pH and to inhalation anesthetics such as halothane (Washburn et al. 2003), both of which influence the breathing rhythm. The conductances of all of these currents are dominated by potassium, and thus their reversal potentials are close both to one another and to the resting potential for pBC cells. This suggests modeling these currents by approximating them with an effective leak current (Guckenheimer et al. 2005), and motivates using the leak parameters g_L, v_L in system (12–19) as active optimization parameters.

Table 3 Empirical data for Cd^{2+}-insensitive pacemakers

	Control	Norepinephrine
Burst duration (s)	$0.44 \pm .02$	0.52 ± 0.05
Frequency (Hz)	0.22 ± 0.05	0.41 ± 0.06
Mean period (ms)	4,546	2,439

Burst period differs between the control and norepinephrine conditions, but the difference in burst duration is not significant. From Table 4 of Viemari and Ramirez (2006)

2.5 Optimization algorithm implementation

The optimization algorithms were implemented using Matlab's optimization toolbox. Results in this paper use the Levenberg–Marquardt algorithm. Objective function gradients were computed using ADMC++ (Phipps 2003), an automatic differentiation package for Matlab. The value of δ in Eq. (4) determines the size of the neighborhood of $\mathcal{M}_0$. This choice will depend upon the separation of time scales in the system. For system (12–19), we take $\delta = 1 \times 10^{-6}$. With this value for δ, system (12–19) is insensitive to the choice of S in Eq. (4). We used (3.33, 1.7) for the diagonal entries of S here, but very different choices of S gave burst timings which differed negligibly.

3 Results

The periodic bursting trajectory for system (12–19) with parameter values given in Table 2 is shown in Fig. 2(a). The located burst events using Eqs. (3) and (4) are marked by x's. The calculated burst period was 6,846 ms, and burst duration 845 ms.

A common empirical definition of burst duration is width at half-maximal amplitude. Figure 3(a) compares the burst duration for system (12–19) using this definition versus using the initiation and termination defining equations (3–4). The leak conductance g_L is varied on a fine mesh, with all other parameter values given in Table 2. As g_L increases from 2.74 to 2.745 the number of spikes decreases by 1. The change in spike number results in an obvious discontinuity in burst duration when using the width at half-maximal amplitude definition. Under this definition the burst duration is also quite flat following the peak. Burst duration changes more smoothly using the geometric defining equations, and is less flat following the peak.

Figure 3(b) compares burst duration using these two definitions over a wider range of g_L values. The mean difference between the two burst durations is 213 ms. Adding this mean difference to the amplitude-based burst duration is a crude approximation of the geometric burst duration. Figure 3(c) shows the relative error of the shifted amplitude burst duration from the

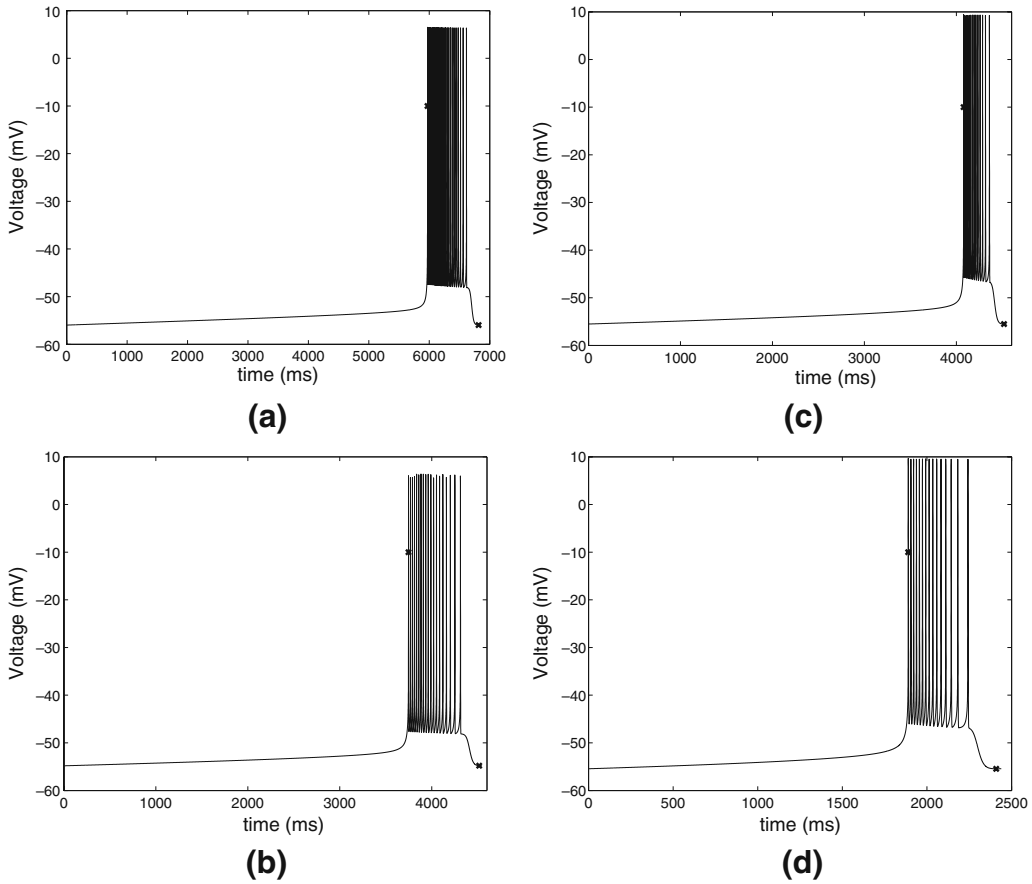

Fig. 2 Four bursting periodic orbits for system (12–19). Burst initiation and termination events are marked by x's. (**a**) Default parameter values, Table 2. (**b**) Set 1, Table 4. (**c**) Control 1, Table 4. (**d**) NE 1, Table 8

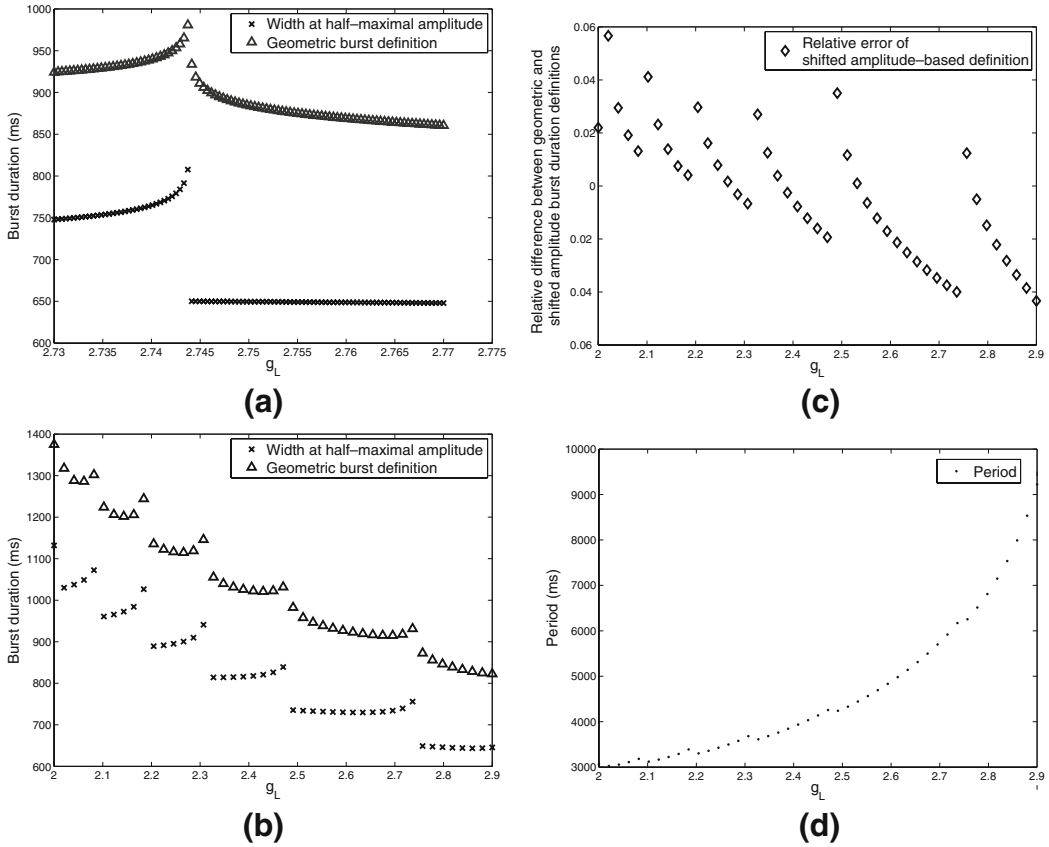

Fig. 3 (**a**–**c**) Comparison of burst durations calculated for system (12–19) across a range of g_L values using the geometric burst defining equations (3–4), versus the width at half-maximal amplitude definition. All other parameter values are given in Table 2. (**a**) Burst duration comparison on a fine g_L mesh near where a change in spike number occurs. (**b**) Burst duration comparison for a wider range of g_L values on a coarser mesh. (**c**) $\frac{BD_{\text{geom}}-BD_{\text{amp}-c}}{BD_{\text{geom}}}$ plotted against g_L, where BD_{geom} is the geometric burst duration, BD_{amp} the amplitude-based burst duration, and $c = 213$ ms. See text. (**d**) Burst period plotted against g_L

geometric burst duration. The calculated relative errors are less than 6%. The burst period ranges from 3,025 ms to 9,220 ms over the g_L values considered in Fig. 3(b) and (c). This is depicted in Fig. 3(d).

3.1 Control data fits

A sequential approach to fitting the burst characteristics reported for Cd^{2+}-insensitive pacemakers in the control setting (see Table 3) was used. This entailed first matching the burst period, and then optimizing burst duration while maintaining a good fit for the period. This was done by first using Eq. (1) with X equal to the burst period and penalty weight $w = 0$, and then setting X to the burst duration, Y the period, and w equal to the reference burst duration.

The leak parameters affect burst period (Butera et al. 1999) and are a likely target of modulation (Section 2.4.2). Thus (g_L, v_L) were selected as the initial active optimization parameters. The observed mean control burst period was 4,546 ms and burst duration averaged 440 ms. We started with an initial burster at $(g_L, v_L) = (2.8, -59.3)$ with period 4,308 ms and burst duration 797 ms. Using our optimization algorithms to fit burst period alone resulted in the parameter values labeled Set 1 in Table 4. The period matches the empirical observations very closely, but the burst duration of 787 ms is longer than the actual 440 ms observed in the control conditions. The voltage trace for Set 1 is shown in Fig. 2(b). The Set 1 parameter values were taken as the starting point for a new optimization using the log penalty function on the period [Eq. (1)]. The parameter sensitivities for the Set 1 burster were used to aid in active parameter selection. Table 5 lists the scaled sensitivities computed using automatic differentiation, together with their rankings by magnitude. The rankings give the index after sorting by magnitude in descending order. We say that a parameter has a high period sensitivity ranking if the period sensitivity to this parameter is large compared with other period sensitivities. High ranking sensitivities correspond to small indices.

A heuristic for adjusting burst duration while keeping the period unchanged is to look for parameters

Table 4 Two parameter sets for system (12–19) obtained from optimization

	Active optimization parameters		Period (ms)	Burst duration (ms)
Set 1	$g_L = 2.8313$	$v_L = -59.3099$	4,546	787
Control 1	$\theta_m = -34.1159$	$\theta_n = -27.2325$	4,548	440
	$\sigma_n = -4.3890$	$\bar{\tau}_n = 9.3977$		
	$\sigma_h = 5.1783$			

Set 1 resulted from attempting to match the period of Cd^{2+}-insensitive pacemakers in the control setting (Table 3), with active parameters g_L, v_L and initial active parameter values (2.8, −59.3). Control 1 the output from attempting to match both period and burst duration for Cd^{2+}-insensitive pacemakers in the control setting, starting from Set 1 with active parameters $\theta_m, \theta_n, \sigma_n, \bar{\tau}_n, \sigma_h$. All other parameter values given in Table 2. X=period, $w = 0$ in Eq. (1) for the Set 1 fit. For Control 1, X=burst duration, $w = 440$, and Y=period

which affect burst duration more strongly than period. This means using parameters with higher burst rank than period rank. The parameters $\theta_m, \sigma_m, \theta_n, \sigma_n, \bar{\tau}_n$, and σ_h all fit this description. The parameter σ_m was discarded because of its low burst sensitivity ranking. Using the remaining five active parameters with objective function (1) resulted in the parameter set labeled as Control 1 in Table 4. Essentially a perfect fit was obtained. The voltage trace is shown in Fig. 2(c).

As an alternative, we select the parameters of the persistent sodium current as active parameters. The persistent sodium current parameter values in system (12–19) are uncertain, motivating use of the $I_{Na(P)}$ parameters for optimization. The parameter set labeled Control 2 in Table 6 shows the results of optimizing over all the $I_{Na(P)}$ parameters. Again a perfect fit was obtained. Figure 4(a–b) shows the discrepancies in period and burst duration over the course of the optimization for Control 2. Convergence occurred after 11 iterations.

In both Control 1 and 2 the relative change in σ_h over the course of the optimization was greater than that for the other active parameters, suggesting that σ_h is important for determining burst characteristics. This was examined further by starting from Set 1 and repeating the optimization using a smaller subset of the $I_{Na(P)}$ parameters which included σ_h. Control 3 shows the results using (θ_h, σ_h), and Control 4 the results from $(g_{Na(P)}, \sigma_h)$ as the active optimization parameters. The resulting fits were substantial improvements from the initial burster corresponding to Set 1: burst duration discrepancies were within 10% for Control 3 and 18% for Control 4, while the period remained within 1% of the empirical observations. Burst duration in the presence of norepinephrine was 520 ms, which was not significantly different from the control burst duration of 440 ms (Table 3; Viemari and Ramirez 2006). The fits from Controls 3 and 4 both deviated less than this from the control burst duration.

Table 5 shows that the relative influence of the potassium current parameters is greater on the burst duration than on the period. Control 5 in Table 6 shows the result of including $\bar{\tau}_n$ together with σ_h in the active optimization parameters. Both $\bar{\tau}_n$ and σ_h changed significantly over the course of the optimization, which yielded an excellent fit.

Neuromodulators often act by altering conductances. This possibility was examined by optimizing over all conductances. The resulting conductance values are given in Control 6 of Table 6. A perfect fit was obtained. The slow conductances $g_{Na(P)}$ and g_L experienced the greatest relative change over the course of the optimization. The potassium conductance g_K also

Table 5 Parameter sensitivities for the Set 1 burster (Table 4)

Parameter	Scaled sensitivities		T rank	Burst rank
	$\frac{\partial T}{\partial \lambda}$	$\frac{\partial (t_{term} - t_{init})}{\partial \lambda}$		
g_{Na}	-8.11×10^2	-6.16×10^2	17	17
v_{Na}	-8.09×10^2	-7.19×10^2	18	16
θ_m	1.42×10^3	-2.21×10^3	15	10
σ_m	5.61×10^2	-8.03×10^2	19	15
g_K	-2.20×10^3	-1.28×10^3	13	11
v_K	4.83×10^3	3.53×10^3	9	7
θ_n	1.18×10^4	6.87×10^3	7	3
σ_n	1.33×10^3	5.10×10^3	16	5
$\bar{\tau}_n$	-1.88×10^3	-2.67×10^3	14	8
$g_{Na(P)}$	-2.15×10^4	9.44×10^2	5	14
$v_{Na(P)}$	-1.07×10^4	5.92×10^2	8	18
$\theta_{\hat{m}}$	1.26×10^5	-10.62	2	19
$\sigma_{\hat{m}}$	3.54×10^4	5.79×10^3	4	4
θ_h	-5.96×10^4	8.05×10^3	3	2
σ_h	3.59×10^3	4.01×10^3	11	6
$\bar{\tau}_h$	2.79×10^3	1.24×10^3	12	13
g_L	2.07×10^4	-1.24×10^3	6	12
v_L	-1.31×10^5	-2.27×10^4	1	1
C	3.63×10^3	2.21×10^3	10	9

T=period, $t_{term} - t_{init}$=burst duration. Scale factors correspond to the parameter values in Table 2

Table 6 Obtained fits for system (12–19) to Cd^{2+}-insensitive pacemaker data in the control setting (Table 3)

	Active optimization parameters		Period (ms)	Burst duration (ms)
Control 2	$g_{Na(P)} = 2.7880$	$v_{Na(P)} = 50.0004$	4,546	440
	$\theta_{\hat{m}} = -39.9066$	$\sigma_{\hat{m}} = -5.8644$		
	$\theta_h = -48.1844$	$\sigma_h = 4.8049$		
	$\bar{\tau}_h = 1.0000 \times 10^4$			
Control 3	$\theta_h = -48.9104$	$\sigma_h = 5.1514$	4,531	482
Control 4	$g_{Na(P)} = 2.6539$	$\sigma_h = 5.1579$	4,516	516
Control 5	$\bar{\tau}_n = 6.1802$	$\sigma_h = 4.2717$	4,466	446
Control 6	$g_{Na} = 29.0386$	$g_K = 16.2096$	4,546	440
	$g_{Na(P)} = 5.3177$	$g_L = 5.7035$		
Control 7	$g_{Na(P)} = 6.9680$	$g_L = 6.8818$	4,584	483
Control 8	$g_L = 3.1510$	$v_L = -58.5762$	4,952	638

Initial parameters correspond to Set 1 in Table 4. X=burst duration, Y=period, $w = 440$ in Eq. (1) for all fits

experienced a large relative change of 45%, whereas the fast sodium conductance changed by less than 4%. Optimizing over the slow conductances alone resulted in a good fit to the control data, as given by Control 7.

Leak channel modulation is one of the primary known modulatory mechanisms in the pBC (Section 2.4.2). However, using (g_L, v_L) as active parameters to try to fit the control data from Set 1 resulted in a poor fit, labeled Control 8 in Table 6. The final burst duration was 638 ms, much greater than the desired 440 ms. Of the fits reported in Table 6, the Control 8 period was also the farthest from the mean observed control period.

The Control 1–8 fits were also performed with finite differences, both using Taylor series integration and Matlab's `ode15s` solver. The Controls 2–7 fits were very similar irrespective of the derivative method. The finite difference fits for Control 1 were worse than the fit using automatic differentiation, with final periods of 3,127 (`ode15s`) and 3,128 (Taylor) ms and final burst

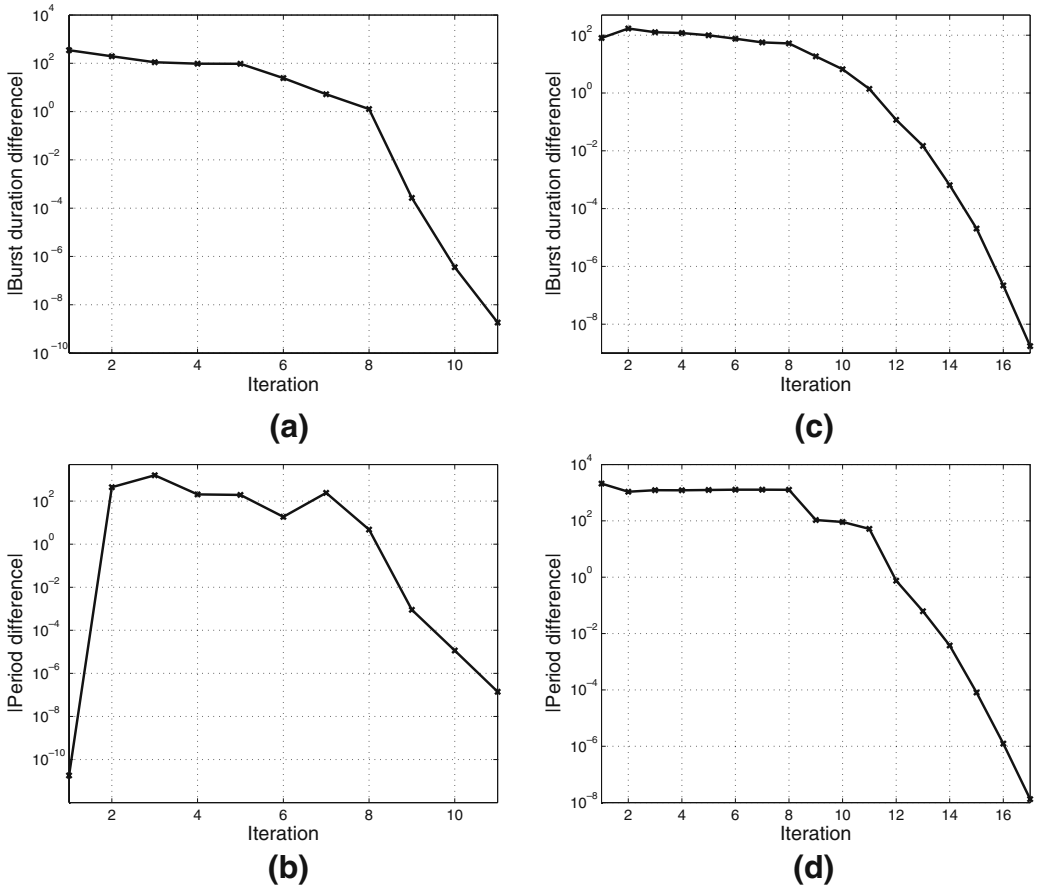

Fig. 4 Progress of two optimization runs. (**a**–**b**) Optimization run resulting in Control 2, Table 6. X=burst duration, Y=period in Eq. (1). (**c**–**d**) Optimization run resulting in NE 6, Table 8. X=period, Y=burst duration in Eq. (1). Time measured in milliseconds

Table 7 Parameter sensitivities for the Control 1 burster (Table 4)

Parameter	Scaled sensitivities		T rank	Burst rank
	$\frac{\partial T}{\partial \lambda}$	$\frac{\partial (t_{\text{term}} - t_{\text{init}})}{\partial \lambda}$		
g_{Na}	5.22×10^2	1.31×10^2	17	16
v_{Na}	7.56×10^2	2.23×10^2	16	15
θ_m	5.06×10^3	1.99×10^3	10	3
σ_m	1.66×10^3	4.41×10^2	12	10
g_{K}	-80.36	5.54×10^2	19	5
v_{K}	-9.23×10^2	-1.31×10^3	15	6
θ_n	1.37×10^3	-2.98×10^3	14	2
σ_n	-6.44×10^3	-8.45×10^2	8	7
$\bar{\tau}_n$	2.82×10^3	8.10×10^2	11	8
$g_{\text{Na(P)}}$	-1.77×10^4	-63.43	5	17
$v_{\text{Na(P)}}$	-8.82×10^3	-62.48	7	18
$\theta_{\hat{m}}$	9.71×10^4	-1.61×10^3	1	5
$\sigma_{\hat{m}}$	2.05×10^4	-1.71×10^3	4	4
θ_h	-6.19×10^4	-4.36×10^2	3	11
σ_h	-5.71×10^3	-2.69×10^2	9	14
$\bar{\tau}_h$	1.59×10^3	-40.62	13	19
g_{L}	1.68×10^4	-3.32×10^2	6	12
v_{L}	-6.96×10^4	6.35×10^3	2	1
C	3.03×10^2	-2.86×10^2	18	13

Scale factors correspond to the parameter values in Table 2

duration 475 ms. Using finite differences and `ode15s` for Control 8 resulted in a poor fit, with final period 5,025 ms and burst duration 656 ms. However, finite differences and Taylor series integration performed well for Control 8, with the final active parameter values $(g_{\text{L}}, v_{\text{L}}) = (3.5105, -57.2746)$ giving the desired period (4,546 ms) and burst duration (440 ms). A complete listing of the results using finite differences is given in the Supplementary Materials.

3.2 Norepinephrine data fits

Norepinephrine application to Cd^{2+}-insensitive pacemakers caused burst period to shorten, but did not significantly alter burst duration (Table 3, Viemari and Ramirez 2006). We examined different mechanisms for this change by starting from one of the obtained fits to the control data discussed in Section 3.1, and using our optimization algorithms to match the burst characteristics under norepinephrine application. In the objective function (1), X was set to the period, Y the burst duration, and w the reference period. Parameter sets Controls 1–2 and 5–6 in Tables 4 and 6 were all excellent fits to the control data. We selected Control 1 as the starting point for optimization, but could just as easily have used Controls 2, 5, or 6 as well.

Table 7 gives the burst characteristic sensitivities for the Control 1 burster. The highest period sensitivity rankings correspond to slow current ($I_{\text{Na(P)}}$, I_L) parameters. The parameters which have higher period sensitivity rankings than burst duration sensitivity rankings are $g_{\text{Na(P)}}$, $v_{\text{Na(P)}}$, $\theta_{\hat{m}}$, θ_h, σ_h, $\bar{\tau}_h$, and g_{L}. As conductances are a common modulatory target, we selected $g_{\text{Na(P)}}$ and g_{L} from this set for optimization. The resulting output is labeled as NE 1 in Table 8, and the voltage trace is shown in Fig. 2(d). A perfect fit to the observed period and burst duration was obtained. This importance of the slow conductances was also demonstrated when all of the conductances were used as active parameters, as shown in NE 2 of Table 8. A perfect fit was again obtained, with the largest relative changes in the active parameter values occurring for $g_{\text{Na(P)}}$ and g_{L}. Note that the relative change in g_{K} was small, in contrast to the fit for burst duration with constrained period obtained in Control 6 (Table 6). Varying the leak parameters g_{L}, v_{L} was another way to match the observed burst characteristics in the norepinephrine condition. The parameter set NE 3 in Table 8 shows the final parameter values obtained using g_{L}, v_{L} as the active parameters. An exact match was obtained, in contrast with attempts to fit the control data using these parameters (Control 8). On the other hand, varying $(\bar{\tau}_n, \sigma_h)$ resulted in an excellent fit to the control data. Attempting to fit the

Table 8 Obtained fits for system (12–19) to Cd^{2+}-insensitive pacemaker data after norepinephrine application (Table 3)

	Active optimization parameters		Period (ms)	Burst duration (ms)
NE 1	$g_{\text{Na(P)}} = 3.1389$	$g_{\text{L}} = 2.4504$	2,439	520
NE 2	$g_{\text{Na}} = 28.0203$	$g_{\text{K}} = 11.3725$	2,439	520
	$g_{\text{Na(P)}} = 2.9282$	$g_{\text{L}} = 2.3317$		
NE 3	$g_{\text{L}} = 2.4125$	$v_{\text{L}} = -58.7136$	2,439	520
NE 4	$g_{\text{Na(P)}} = 3.0055$	$\theta_{\hat{m}} = -40.1244$	2,439	520
	$\sigma_{\hat{m}} = -6.3893$	$\theta_h = -47.9642$		
	$\sigma_h = 5.1597$	$\bar{\tau}_h = 1.0000 \times 10^4$		
NE 5	$g_{\text{Na(P)}} = 3.6095$	$\sigma_h = 5.2835$	2,439	520
NE 6	$\theta_h = -44.3301$	$\sigma_h = 4.7354$	2,439	520
NE 7	$\bar{\tau}_n = 9.8538$	$\sigma_h = 5.3777$	4, 528	494

Initial parameters correspond to Control 1 in Table 4. X=period, Y=burst duration, $w = 2, 439$ for all fits

norepinephrine data using $(\bar{\tau}_n, \sigma_h)$ resulted in a poor fit (NE 7).

Persistent sodium current parameters could also be used to match the norepinephrine data. Perfect fits were obtained when using $g_{\mathrm{Na(P)}}, \theta_{\hat{m}}, \sigma_{\hat{m}}, \theta_h, \sigma_h, \bar{\tau}_h$ as active parameters, as shown in NE 4, Table 8. An exact match was still obtained when the active parameter set was reduced to $(g_{\mathrm{Na(P)}}, \sigma_h)$, corresponding to NE 5, or to (θ_h, σ_h), labeled NE 6 in Table 8. The discrepancies in period and burst duration over the course of the optimization for NE 6 are shown in Fig. 4(c–d).

The NE 1–7 fits were repeated using finite differences with both Taylor series integration and Matlab's `ode15s` solver. In all cases, the resulting fits were very similar to those using automatic differentiation. These results are given in the Supplementary Materials.

4 Discussion

Viemari and Ramirez (2006) observed that burst duration and period in pBC pacemaker cells can be controlled independently of one another. Fitting Butera et al.'s (1999) model to the empirical data shows some of the ways this can be accomplished. Excellent fits can be obtained in a number of ways. For example, the control data can be fit by adjusting a collection of activation and time constant parameters from all the currents (Control 1, Table 4), all parameters of the persistent sodium current (Control 2, Table 6), time constant and activation parameters for potassium and persistent sodium inactivation (Control 5), and conductances for all currents in the model (Control 6). The results give insight into the relative importance of different parameters in shaping burst characteristics. For example, Control 2 varied 7 parameters but the relative change in σ_h was by far the largest over the course of the optimization, suggesting that σ_h is important for altering burst duration when the period is constrained. This is supported by subsequent optimization runs which included σ_h in a smaller set of parameters (e.g. Control 5), where excellent fits were still obtained. This steepness at half-activation parameter has not been emphasized in previous studies.

One of the objectives of this study was to examine possible roles of the persistent sodium current in shaping bursts. From Control 2 we see that $I_{\mathrm{Na(P)}}$ can modify burst duration without changing burst period. The inactivation kinetics appear to be particularly important. The persistent sodium current can also modulate burst period when the burst duration is constrained. This is seen in NE 4, where a perfect fit to the norepinephrine data was obtained by modulating $I_{\mathrm{Na(P)}}$ parameters. However, here the largest relative changes occurred for $g_{\mathrm{Na(P)}}$ and $\theta_{\hat{m}}$, whereas σ_h changed much less. The results for NE 1, 2, and 4 in Table 8 suggest that changes in the slow conductances $g_{\mathrm{Na(P)}}, g_{\mathrm{L}}$ are a ready means for modulating period independent of burst duration. This is supported by the sensitivities in Table 7. The parameters $g_{\mathrm{Na(P)}}, v_{\mathrm{Na(P)}}, \theta_{\hat{m}}, \theta_h, \sigma_h, \bar{\tau}_h$,and g_{L} all have higher ranking period sensitivities than burst duration sensitivities. Within this set, the period is least sensitive to σ_h and $\bar{\tau}_h$. For both Set 1 and Control 1, the slow conductances have period sensitivity rankings in the top third (Tables 5 and 7).

On the other hand, for both Set 1 and Control 1 the potassium current parameters have higher burst duration sensitivity rankings than period sensitivity rankings. This is consistent with Ghigliazza and Holmes (2004), who found that changing the potassium current time scale in the SRK model (Sherman et al. 1988) could strongly affect the number of spikes per burst while only moderately affecting burst period. The fast sodium activation parameters θ_m, σ_m also appear to affect burst duration more strongly than period. The period and burst duration are both very sensitive to the leak reversal potential. This is true for both Set 1 and Control 1. Varying the leak parameters $g_{\mathrm{L}}, v_{\mathrm{L}}$ resulted in a perfect fit to the burst characteristics in the presence of norepinephrine (NE 3). Recall that the leak current can be viewed as an amalgamation of currents with very slow time constants that change little over a period of the bursting oscillations. Thus varying the leak parameters is a likely modulatory mechanism for altering burst period with minimal disturbance to burst duration. It may be more difficult to use the leak parameters to alter burst duration while respecting constraints on the period (see Control 8). Likely candidates for modulating burst duration independently of period include the delayed rectifier potassium currents (currents which operate on the middle time scale), and time scale parameters for slow processes such as persistent sodium current inactivation.

Much of the neural parameter estimation literature uses global optimization or search methods (Bhalla and Bower 1993; Foster et al. 1993; Prinz et al. 2003; Vanier and Bower 1999). The methods presented here are local methods which use the geometry underlying bursting to introduce burst event defining equations. These defining equations are then used to fit burst characteristics. This approach is new, combining optimization methods with fast-slow decompositions of model equation burst trajectories. A complication is that the phase space geometry is not empirically observable. Thus the

burst termination event as defined in Eq. (4) is not directly observable either. In practice the experimenter will have to use some other measure to compute the burst duration from the observed voltage trace. Simple measures such as adding a constant to the width at half-maximal amplitude may match the geometric definition reasonably well (Fig. 3). Detailed examination of empirical burst duration measures and the quality of parameter estimates that result from using geometric features to fit these empirical measures will be very helpful.

Using geometric features in optimization algorithms can be useful even when biased parameter estimates result. In many biological situations, the aim of modeling is to gain insight into different mechanisms underlying observed behavior, rather than finding a set of equations and parameter values which exactly describe the system. It is extremely rare to be in a situation where the form of the ODE model is thought to be completely correct. Currents which are known to be present are regularly omitted from Hodgkin–Huxley style models. For example, Butera, Rinzel, and Smith's model of the pBC omits calcium currents which are known to exist. In this case some bias in the parameter estimates is acceptable, as the estimation and sensitivity analysis can still be used to tease apart the roles of different currents in controlling features such as period and burst duration. This is the approach we have taken here. Modifications continue to be made to Butera et al.'s model as new experimental data become available (Rybak et al. 2004). The methods presented in this paper can be used to aid model development and exploration.

One of the challenges of parameter estimation for bursting models is that spike number often changes through highly sensitive canard trajectories (Terman 1991). The geometric burst termination defining equation (4) is advantageous in this situation, as can be seen in Fig. 3(a). As g_L is increased from 2.74 to 2.745, the final interspike interval increases until finally the last spike is lost and the number of spikes decreases by one. A depolarized voltage "shoulder" corresponding to a canard persists after the spike number has changed. The width of this shoulder decreases as g_L is further increased. The geometric defining equation reflects the amount of time the trajectory spends near the saddle portion of the critical manifold. As a consequence, burst duration varies smoothly near where the change in spike number occurs, and the burst duration slope indicates whether the width of the voltage shoulder is increasing or decreasing with the parameter. On the other hand, the width at half-maximal amplitude definition of burst duration does not capture how the width of the voltage shoulder varies following the change in spike number. This results in both a large, discontinuous jump in burst duration when spike number changes, and in a nearly flat region following the change in spike number. Both the jagged and flat portions of the amplitude-based burst duration plot in Fig. 3(a) can cause difficulties for gradient-based optimization algorithms.

Several of the objective functions in the literature involve spike number (Bhalla and Bower 1993; Vanier and Bower 1999), and thus change discontinuously. Other objective functions involve smoothing (Hayes et al. 2005) or transforming (Tabak et al. 2000) the time series data. The objective functions we use are simple ones based directly upon fundamental, biologically relevant quantities such as period and burst duration. This makes the progress of the optimization algorithms easier to interpret. The algorithms converge after a small number of iterations (Fig. 4). Different objective functions besides Eq. (1) involving the period and burst duration are possible, depending upon the available data and goals of the research. The period and burst duration can be combined with other features of the voltage trace. Casey (2004) combined period and the voltage time series for spiking data. The objective function there involved voltage least squares on a rescaled, common time axis, together with a log penalty on period discrepancies. A similar approach using both period and burst duration together with the voltage time series is possible for bursting data. Fitting the period and burst duration can also serve as a way to generate initial parameter values for subsequent optimization involving more detailed features of the data.

An appealing feature of using gradient-based optimization algorithms is that the parameter sensitivities involved are biologically relevant and easily interpreted. Here we have used automatic differentiation and Taylor series integration to accurately compute gradients, but it is worth noting that the geometrical ideas are independent of the numerical method used. [1] There has been little published work on how gradient accuracy affects optimization algorithm performance for ODE models. More work is needed to examine if and when substantial accuracy is necessary for the optimization algorithms to work well. Our work with the pBC and other bursting models indicates that the numerical method can play a role when solutions are

[1] A Matlab implementation using finite differences is available in the online Supplementary Materials.

highly sensitive to the parameters, for example near where spikes are added or subtracted. We illustrate this in the context of continuation of periodic orbits with fixed period.

Let $D_\lambda T$ denote the Jacobian of the period with respect to parameters. The entries of $D_\lambda T$ consist of the period sensitivities. The kernel of $D_\lambda T$ gives the parameter tangent space of $\mathcal{M}_T$, the manifold of periodic orbits with fixed period T. This information can be used in a predictor-corrector framework for continuation. Figure 5 shows an example for continuation of fixed period orbits in the (g_L, v_L) plane. The number of spikes stays constant as we move from point A to B in Fig. 5, but at point B we are close to adding a spike. The degree to which period and burst duration sensitivities differ when different numerical methods are used depends upon how close the system is to adding or dropping a spike. The relative error at point A of scaled sensitivities calculated using finite differences versus automatic differentiation is less than 3×10^{-4}. At $(g_L, v_L) = (2.7183, -58.0967)$, the relative error is $\mathcal{O}(1)$.

Canards associated with changes in spike number occur in thin regions of parameter space. The frequency that optimization algorithms land in these thin regions and their effect on the optimization need further examination. Of the Controls 1–8 optimization runs described in Section 3.1, the numerical method used had a large effect on the final parameters in Controls 1 and 8. The optimization algorithms likely encountered canard trajectories during these two runs. Situations can also arise where regions of the objective function landscape are nearly flat. In this case high accuracy may be needed for the optimization algorithms to properly make their way towards a minimum. Tien (2007) describes a test problem where using finite differences fails due to this reason, but using automatic differentiation leads to the global minimum.

Continuing families of periodic orbits is often itself of interest. Comparing the trajectories from points A and B in Fig. 5(a), we see that burst duration changes significantly over $\mathcal{M}_T$ [Fig. 5(b–c)]. The kernel of $D_\lambda(t_{\text{term}} - t_{\text{init}})$ gives the parameter tangent space of the manifold of periodic orbits with constant burst

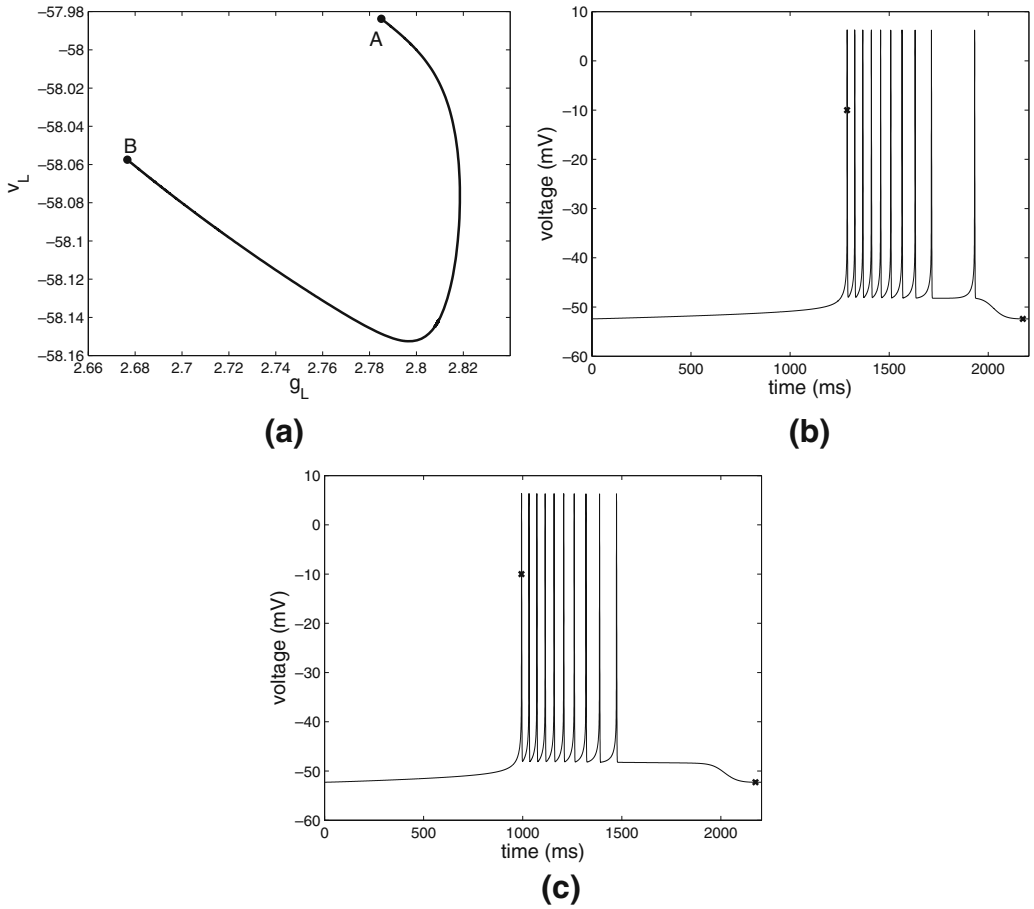

Fig. 5 Continuation of fixed period bursters for system (12–19) in the (g_L, v_L) plane. All other parameter values given in Table 2. (**a**) The manifold $\mathcal{M}_T$ of fixed period bursters. (**b**) Burst orbit at point A of $\mathcal{M}_T$. (**c**) Burst orbit at point B of $\mathcal{M}_T$

duration. The intersection of these two manifolds gives the submanifold of fixed period and burst duration orbits.

Predictor-corrector continuation tends to follow burst families with a fixed number of spikes (Fig. 5). On the other hand, spike number does change during optimization when using penalty functions such as Eq. (1) to fit the control data. For example, Set 1 has 19 spikes while Control 1 has 14 (Fig. 2). Figure 4 shows discrepancies in burst duration and period over the course of the optimization runs which terminate at Control 2 and NE 6. For Control 2 the log penalty term in (1) involves the period, whereas in the NE 6 optimization run burst duration discrepancies are penalized. In both cases we see that the penalty initially increases before eventually decreasing. This initial increase allows for changes in spike number.

We expect the idea of using geometrical features of the ODE to aid in parameter estimation to be broadly applicable. Bursting models typically have a separation of time scales which we utilize in our methods. Combining basic dynamical features such as periodic orbits into optimization algorithms has largely been unexplored. In addition to the work presented here on periodic bursting in the pBC, we have also used this approach for transient bursts in the Hindmarsh–Rose equations (Hindmarsh and Rose 1984). Focusing on burst timing rather than on the entire voltage trace greatly simplifies objective function landscapes there (Tien 2007). Both Butera et al.'s model and the Hindmarsh–Rose equations are square-wave bursters with a single slow variable. It would be interesting to adapt the methods used here to other types of bursters, and to models with multiple slow variables. Application to synaptically coupled cells is also of interest.

Acknowledgements This work was partially supported by grants from the Department of Energy, the National Science Foundation and the National Institutes of Health. The authors thank Eric Phipps for assistance with ADMC++, and the anonymous reviewers for many helpful suggestions and criticisms.

Appendix

A periodic orbit is *elementary* if it has a single multiplier of modulus one. Here we prove that $D_\Delta F$ as given in Eq. (10) has full rank when evaluated at an elementary periodic orbit with transverse events.

Proposition 1 *Let F be given by Eq. (6), and $D_\Delta F$ by Eq. (10). If $D_\Delta F$ is evaluated at a periodic orbit with a single multiplier of modulus* 1*, and $<\nabla\Gamma_{\sigma_i}, f(z_{\sigma_i})> \neq 0$ for $i = 1, \ldots, n_e$, then $D_\Delta F$ has full rank.*

Proof Let A denote the submatrix given by the first $m \cdot zdim$ rows of Eq. (10), B consist of rows $m \cdot zdim + 1$ through $m \cdot zdim + n_e$, and C denote the last $m - n_e$ rows. B corresponds to the rows of $D_\Delta F$ containing the $\nabla\Gamma_{\sigma_i}$ terms, and C the v_{ρ_j} elements of Eq. (10).

Guckenheimer and Meloon (2000) show that A has full rank for elementary periodic orbits. Because $<\nabla\Gamma_{\sigma_i}, f(z_{\sigma_i})> \neq 0$, $\nabla\Gamma_{\sigma_i} \neq 0$ and the rows of B are therefore linearly independent. We next show that transverse events imply that each row of B has a nonzero component in $N(A)$. The inner product of $\nabla\Gamma_{\sigma_i}$ with v_{σ_i}, the basis element of $N(A)$ corresponding to sliding mesh point σ_i along the orbit, is equal to $< f(z_{\sigma_i}), \nabla\Gamma_{\sigma_i} >$. This is nonzero by the transversality assumption. Let $[A; B]$ denote the first $m \cdot zdim + n_e$ rows of $D_\Delta F$. We thus have that $[A; B]$ has full rank. Finally, note that a basis for the nullspace of $[A; B]$ is given by the basis elements of $N(A)$ corresponding to sliding non-event points along the periodic orbit. These basis elements are the rows of C. □

Similar results hold for transient burst solutions. In this case Δ consists of the event time points together with all the phase space points, with non-event time points being treated as fixed. The shooting map F is modified to remove the periodic boundary condition. In this case the corresponding expression for $D_\Delta F$ has full rank when evaluated at a solution trajectory with transverse events. Details are given in Tien (2007).

References

Bhalla, U., & Bower, J. (1993). Exploring parameter space in detailed single neuron models: Simulations of the mitral and granule cells of the olfactory bulb. *Journal of Neurophysiology 69*(6), 1948–1965.

Bickmeyer, U., Heine, M., Manzke, T., & Richter, D. (2002). Differential modulation of I_h by 5-HT receptors in mouse CA1 hippocampal neurons. *European Journal of Neuroscience 16*, 209–218.

Butera, R. J., Rinzel, J., & Smith, J. C. (1999). Models of respiratory rhythm generation in the pre-Bötzinger complex. I. Bursting pacemaker neurons. *Journal of Neurophysiology 81*, 382–397.

Casey, R. (2004). *Periodic orbits in neural models: Sensitivity analysis and algorithms for parameter estimation.* PhD Thesis, Cornell University.

Crill, W. (1996). Persistent sodium current in mammalian central neurons. *Annual Review of Physiology 58*, 349–362.

Deisz, R., Fortin, G., & Zieglgansberger, W. (1991). Voltage dependence of excitatory postsynaptic potentials of rat neocortical neurons. *Journal of Neurophysiology 65*, 371–382.

Feldman, J. L., Mitchell, G. S., & Nattie, E. E. (2003). Breathing: rhythmicity, plasticity, chemosensitivity. *Annual Review of Neuroscience 26*, 239–266.

Fletcher, R. (1987). *Practical methods of optimization.* Chichester: John Wiley and Sons.

Foster, W., Ungar, L., & Schwaber, J. (1993). Significance of conductances in Hodgkin–Huxley models. *Journal of Neurophysiology 70*(6), 2502–2518.

Ghigliazza, R., & Holmes, P. (2004). Minimal models of bursting neurons: How multiple currents, conductances, and timescales affect bifurcation diagrams. *SIAM Journal on Applied Dynamical Systems 3*(4), 636–670.

Griewank, A. (2000). *Evaluating derivatives: Principles and techniques of automatic differentiation*. Philadelphia: SIAM.

Guckenheimer, J., & Meloon, B. (2000). Computing periodic orbits and their bifurcations with automatic differentiation. *SIAM Journal on Scientific Computing 22*(3), 951–985.

Guckenheimer, J., Tien, J. H., & Willms, A. (2005). Bifurcations in the fast dynamics of neurons: implications for bursting. In S. Coombes & P. C. Bresloff (Eds.), *Bursting: the genesis of rhythm in the nervous system.* New Jersey: World Scientific Publishing Co.

Haller, M., Mironov, S., Karschin, A., & Richter, D. (2001). Dynamic activation of K_{ATP} channels in rhythmically active neurons. *Journal of Physiology 537*(1), 69–81.

Hayes, R., Byrne, J., Cox, S., & Baxter, D. (2005). Estimation of single-neuron model parameters from spike train data. *Neurocomputing 65*, 517–529.

Hille, B. (2001). *Ion channels of excitable membranes.*, (3rd ed.). Sunderland, MA: Sinauer.

Hindmarsh, J., & Rose, R. (1984). A model of neuronal bursting using 3 coupled 1st order differential equations. *Proceedings of the Royal Society of London Series B 221*(1222), 87–102.

Johnson, S., Smith, J., Funk, G., & Feldman, J. (1994). Pacemaker behavior of respiratory neurons in medullary slices from neonatal rat. *Journal of Neurophysiology 72*, 2598–2608.

Jones, C. K. R. T. (1995). Geometric singular perturbation theory. *Lecture Notes in Mathematics 1609*, 44–118.

Kinkead, R., Bach, K., Johnson, S., Hodgeman, B., & Mitchell, G. (2001). Plasticity in respiratory motor control: Intermittent hypoxia and hypercapnia activate opposing serotonergic and noradrenergic modulatory systems. *Comparative Biochemistry and Physiology A. Molecular and Integrative Physiology 130*, 207–218.

Koshiya, N., & Smith, J. C. (1999). Neuronal pacemaker for breathing visualized in vitro. *Nature 400*, 360–363.

Magistretti, J., & Alonso, A. (1999). Biophysical properties and slow voltage-dependent inactivation of a sustained sodium current in entorhinal cortex layer-II principal neurons. *Journal of General Physiology 114*, 491–509.

Mironov, S., Hartelt, N., & Ivannikov, M. (2005). Mitochondrial K_{ATP} channels in respiratory neurons and their role in hypoxic facilitation of rhythmic activity. *Brain Research 1033*, 20–27.

Onimaru, H., Arata, A., & Homma, I. (1989). Firing properties of respiratory rhythm generating neurons in the absence of synaptic transmission in rat medulla in vitro. *Experimental Brain Research 76*, 530–536.

Phipps, E. T. (2003). *Taylor series integration of differential-algebraic equations: Automatic differentiation as a tool for simulating rigid body mechanical systems.* Ph.D. Thesis, Cornell University.

Prinz, A. A., Billimoria, C. P., & Marder, E. (2003). Alternative to hand-tuning conductance-based models: Construction and analysis of databases of model neurons. *Journal of Neurophysiology 90*, 3998–4015.

Richter, D., Manzke, T., Wiklen, B., & Ponimaskin, E. (2003). Serotonin receptors: Guardians of stable breathing. *Trends in Molecular Medicine 9*(12), 542–548.

Rinzel, J., & Lee, Y. S. (1987). Dissection of a model for neuronal parabolic bursting. *Journal of Mathematical Biology 25*, 653–675.

Rybak, I. A., Shevtsova, N. A., Ptak, K., & McCrimmon, D. R. (2004). Intrinsic bursting activity in the pre-Bötzinger complex: Role of persistent sodium and potassium currents. *Biological Cybernetics 90*, 59–74.

Sherman, A., Rinzel, J., & Keizer, J. (1988). Emergence of organized bursting in clusters of pancreatic beta cells by channel sharing. *Biophysical Journal 54*, 411–425.

Smith, J., Ellenberger, H., Ballanyi, K., Richter, D., & Feldman, J. (1991). Pre-Bötzinger complex: A brainstem region that may generate respiratory rhythm in mammals. *Science 254*, 726–729.

Tabak, J., Murphey, C., & Moore, L. (2000). Parameter estimation methods for single neuron models. *Journal of Computational Neuroscience 9*(3), 215–236.

Terman, D. (1991). Chaotic spikes arising from a model of bursting in excitable membranes. *SIAM Journal on Applied Mathematics 51*(5), 1418–1450.

Thoby-Brisson, M., Cauli, B., Champagnat, J., Fortin, G., & Katz, D. (2003). Expression of functional tyrosine kinase B receptors by rhythmically active respiratory neurons in the preBotzinger complex of neonatal mice. *Journal of Neuroscience 23*(20), 7685–7689.

Tien, J. H. (2007). *Optimization for bursting neural models.* Ph.D. Thesis, Cornell University.

Vanier, M. C., & Bower, J. M. (1999). A comparative survey of automated parameter-search methods for compartmental neural models. *Journal of Computational Neuroscience 7*, 149–171.

Viemari, J., & Ramirez, J. (2006). Norepinephrine differentially modulates different types of respiratory pacemaker and nonpacemaker neurons. *Journal of Neurophysiology 95*(4), 2070–2082.

Washburn, C., Bayliss, D., & Guyenet, P. (2003). Cardiorespiratory neurons of the rat ventrolateral medulla contain TASK-1 and TASK-3 channel mRNA. *Respiratory Physiology and Neurobiology 138*, 19–35.

Washburn, C., Sirois, J., Talley, E., Guyenet, P., & Bayliss, D. (2002). Serotonergic raphe neurons express TASK channel transcripts and a TASK-like pH- and halothane-sensitive K^+ conductance. *Journal of Neuroscience 22*(4), 1256–1265.